Curvature-Induced Twist in Homeotropic Nematic Tori

Perry W. Ellis, Karthik Nayani, James P. McInerney, D. Zeb Rocklin, Jung Ok Park, Mohan Srinivasarao, Elisabetta A. Matsumoto, and Alberto Fernandez-Nieves

Phys. Rev. Lett. **121**, 247803 — Published 14 December 2018

DOI: 10.1103/PhysRevLett.121.247803

Curvature-induced twist in homeotropic nematic tori

Perry W. Ellis,[1,2,*] Karthik Nayani,[3,4,*] James P. McInerney,[1] D. Zeb Rocklin,[1] Jung Ok Park,[3] Mohan Srinivasarao,[3] Elisabetta A. Matsumoto,[1] and Alberto Fernandez-Nieves[1,5,6]

[1] *School of Physics, Georgia Institute of Technology, Atlanta, GA, 30332-0430*
[2] *Present address: John A. Paulson School of Engineering and Applied Sciences, Harvard University, Cambridge, Massachusetts, 02138*
[3] *School of Materials Science and Engineering, Georgia Institute of Technology, Atlanta, GA, 30332-0245*
[4] *Present address: Department of Chemical and Biological Engineering, University of Wisconsin-Madison, Madison, Wisconsin, 53706-1691*
[5] *Department of Condensed Matter Physics, University of Barcelona, 08028 Barcelona, Spain*
[6] *ICREA-Institució Catalana de Recerca i Estudis Avançats, 08010 Barcelona, Spain*

(Dated: November 14, 2018)

We confine a nematic liquid crystal with homeotropic anchoring to stable toroidal droplets and study how geometry affects the equilibrium director configuration. In contrast to the case of cylindrical confinement, we find that the equilibrium state is chiral - a twisted and escaped radial director configuration. Furthermore, we find that the magnitude of the twist distortion increases as the ratio of the ring radius to the tube radius decreases; we confirm this with computer simulations of optically polarized microscopy textures. In addition, numerical calculations also indicate that the local geometry indeed affects the magnitude of the twist distortion. We further confirm this curvature-induced twisting using bent cylindrical capillaries.

A system with broken reflection symmetry cannot be superimposed onto its reflection using only translations and rotations; it has a handedness and thus is chiral [1]. Chirality can appear in systems comprised of chiral building blocks, as in some photonic metamaterials [2], or quite remarkably, via spontaneous symmetry breaking in an achiral system [3]. This latter scenario is often studied in nematic liquid crystals (NLC), an ordered material where the constituent particles are achiral [4–14], anisotropic, and preferentially align parallel to each other. This common direction is referred to as the director, $\mathbf{n}$. The well-known Frank-Oseen free energy describes the cost of splay, twist, bend, and saddle-splay distortions of $\mathbf{n}$: $F = (1/2)\int \mathrm{d}V\,\{K_{11}(\nabla\cdot\mathbf{n})^2 + K_{22}(\mathbf{n}\cdot\nabla\times\mathbf{n})^2 + K_{33}(\mathbf{n}\times(\nabla\times\mathbf{n}))^2 - (K_{22}+K_{24})\nabla\cdot(\mathbf{n}(\nabla\cdot\mathbf{n}) + \mathbf{n}\times(\nabla\times\mathbf{n}))\}$, where K_{11}, K_{22}, K_{33}, and K_{24} are the corresponding elastic constants. Under toroidal confinement with a director that is everywhere tangential to the surface, the achiral, axial state, shown in Fig. 1(a), is unstable against the doubly-twisted, chiral state, shown in Fig. 1(b), depending on both K_{22}/K_{24} and the aspect ratio of the torus, $\xi = R_0/a$, with R_0 the central ring radius and a the tube radius [see Fig. 2(a)] [10]. Furthermore, whenever reflection symmetry is broken, the magnitude of the resultant twist distortion grows with decreasing ξ, due to, in large measure, the saddle-splay contributions to F, which effectively screen the energetic cost for twisting [10, 15].

This doubly-twisted state is also found for cylindrical confinement when $K_{24} > K_{22}$, despite the fact that simply aligning $\mathbf{n}$ along the long axis of the cylinder would result in a distortion-free state [12, 13]. The key here is again saddle-splay. Importantly, under homeotropic confinement, corresponding to $\mathbf{n}$ being normal to the boundaries of the cylinder, the saddle-splay contribution to F takes a constant value and does not depend on what $\mathbf{n}$ does in the bulk. Correspondingly, the LC adopts an achiral configuration [16, 17], unless $K_{22} \ll K_{11}, K_{33}$ [11], which is true for lyotropic chromonic liquid crystals (LCLC).

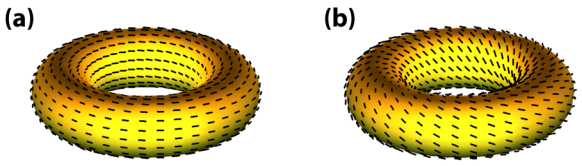

FIG. 1. Director schematics of nematic tori with planar anchoring for an (a) axial and a (b) doubly-twisted director field.

In this Letter, we consider toroidal NLC droplets with homeotropic anchoring using a LC where all the elastic constants are comparable, and show that despite the fact that saddle-splay plays no role in the equilibrium director field, the confinement geometry still induces spontaneous reflection symmetry breaking. Similar to prior results with planar anchoring [10], where saddle-splay is of utmost importance, we also find that the magnitude of the resulting twist distortion increases with decreasing

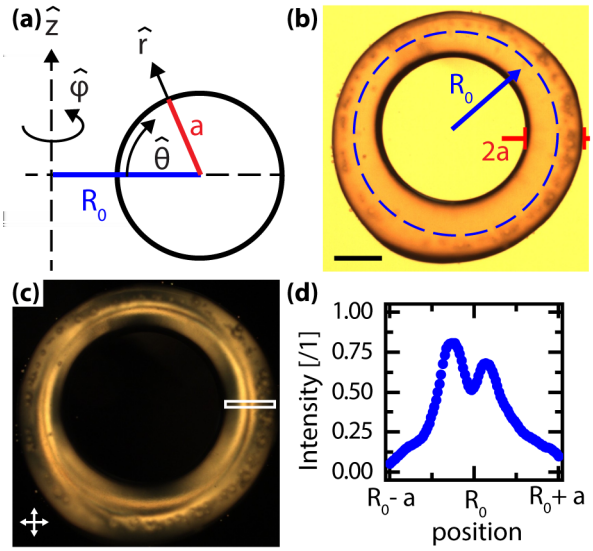

FIG. 2. (a), Schematic detailing the $\{r, \theta, \varphi\}$ toroidal coordinate system, where r is measured from the central ring and θ, and φ are the polar and azimuthal angles in the torus, respectively. We characterize the slenderness, or aspect ratio of the torus with $\xi = R_0/a$, the ratio of the central ring radius, R_0, and the tube radius, a. (b,c), Bright-field and associated crossed-polar microscopy images of an example nematic toroidal droplet with homeotropic anchoring, where $\xi = 5$. Scale bar is 250 μm. (d), Grayscale intensity profile for the region highlighted in (c), where 1 corresponds to white and 0 to black.

ξ, revealing that such a *geometric control* of chirality is *general* and does not depend on boundary conditions. For a given NLC, the geometrically-tuned chirality depends only on ξ, a ratio of curvatures. We confirm this using bent cylindrical capillaries, where by keeping a constant and changing R_0 smoothly, we generate a gradient in the magnitude of the twist distortion. The ability to generate chiral twist gradients is new and opens the door to additional chirality-dependent fundamental studies.

We make stable toroidal droplets with the NLC 4-Cyano-4'-pentylbiphenyl (5CB, Heibei Chemical Co.) in an outer yield-stress medium consisting of a jammed dispersion of polyacrylamide hydrogels (Carbopol ETD 2020, Lubrizol) [18]. The yield-stress medium has approximately 8 mM sodium dodecyl sulfate (SDS, Sigma Aldrich), a concentration that yields strong homeotropic anchoring [19].

We show bright-field and crossed-polar images of a representative toroidal droplet with $\xi = 5$ in Fig. 2(b,c), respectively. In the regions where $\hat{\varphi}$ is aligned along either the polarizer (P) or analyzer (A), the crossed-polarized texture [Fig. 2(c)] has the characteristic dark-light-dark-light-dark pattern associated with the classic escaped radial (ER) configuration of homeotropic cylindrical nematics [16, 17]. This configuration is illustrated schematically in Fig. 3(a). We experimentally generate this configuration by filling a 150 μm inner-diameter (ID) cylindrical capillary (VitroCom) with 5CB. The capillary is coated with lecithin (Granular, Acros) prior to filling to induce homeotropic anchoring [18]. Example bright-field and crossed-polarized images of the capillary are shown in Fig. 3(b,c). Indeed, the same dark-light-dark-light-dark pattern is found in the crossed-polar images of both the toroidal droplet [Fig. 2(c)] and the cylindrical capillary [Fig. 3(c)]. However, when we compare the grayscale intensity profiles [20] taken across the tube of both the toroidal droplet and the cylindrical capillary [highlighted regions, Fig. 2(c) and Fig. 3(c)], plotted in Fig. 2(d) and Fig. 3(d), respectively, we see that there are quantitative differences. Specifically, we note that while both intensity profiles have two maxima surrounding a central minimum, the central minimum in the intensity profile for the cylindrical capillary [Fig. 3(d)] is much lower than the central minimum in the profile for the toroidal droplet [Fig. 2(d)]. We quantify this difference with an intensity ratio, $I_{\max}/I_{\min}$, where $I_{\max}$ is the average of the intensity values of the two maxima and $I_{\min}$ is the intensity value of the central minimum; for the cylindrical capillary with an ER configuration, $I_{\max}/I_{\min} \approx 4$ while for the toroidal droplet, $I_{\max}/I_{\min} \approx 1.6$.

We also fill a 150 μm ID capillary with 31.5% w/w Sunset Yellow (SSY) (90% purity, Sigma Aldrich), a LCLC with $K_{22} \ll K_{11}, K_{33}$ [11, 18]. Before filling, the capillary is coated with Parylene to enforce homeotropic anchoring [18]. Prior experiments showed that this system spontaneously breaks reflection symmetry and twists, adopting a twisted escaped radial (TER) configuration, illustrated schematically in Fig. 3(e) [11].

A bright-field and crossed-polarized image of this experiment is shown in Figs. 3(f,g), respectively. By considering the grayscale intensity profile in the highlighted region in Fig. 3(g) and plotted in Fig. 3(h), we find $I_{\max}/I_{\min} \approx 1.3$. Interestingly, the intensity ratio found with the homeotropic toroid is close to this value. More generally, using a variety of toroids with different ξ and a, we see that $I_{\max}/I_{\min}$ increases with ξ, from the floor provided by the TER configuration in a cylindrical capillary [open square, $\xi = \infty$, Fig. 4(a)] to the ceiling set by the ER configuration in a cylindrical capillary [triangles and square, $\xi = \infty$, Fig. 4(a)]. From this,

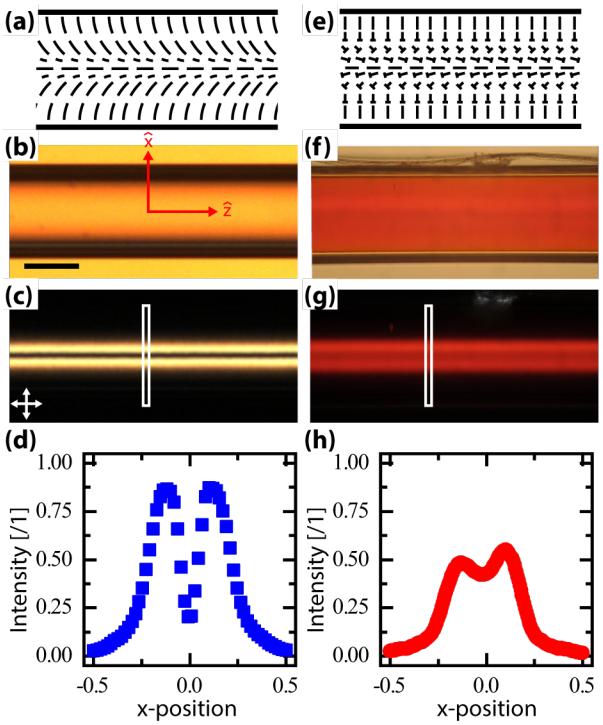

FIG. 3. (a,e) Director schematics, (b,f) bright-field and (c,g) associated crossed-polar microscopy images of an (a–c) escaped radial (ER) configuration and a (e–g) twisted escaped radial (TER) configuration in a cylindrical capillary. The capillaries in (b,c) and (f,g) are filled with 5CB and SSY, respectively, and the scale bar is 100 µm. The nails in (e) represent the director coming out of the page. (d,h), Grayscale intensity profiles for the regions highlighted in (c,g), respectively, where an intensity of 1 corresponds to white and 0 to black.

we hypothesize that although K_{22} is comparable to K_{11} and K_{33} for 5CB, our homeotropic NLC toroids have a TER configuration, with a decreasing twist with increasing ξ.

To test this hypothesis, we first consider the Frank-Oseen free energy with a radially symmetric ansatz in the toroidal coordinate system, $\{r, \theta, \varphi\}$, with $\{r, \theta\}$ polar coordinates in the circular cross section and φ the azimuthal angle in the torus [see Fig. 2(a)]. We define the angles $\alpha = \arctan(\mathbf{n}\cdot\hat{\theta}/\mathbf{n}\cdot\hat{r})$ and $\beta = \arctan(\mathbf{n}\cdot\hat{\varphi})$, describing the director orientation in the $r\theta$-plane and $r\varphi$-plane, respectively. With this parameterization, we have $\mathbf{n} = \hat{r}\cos\alpha\sin\beta + \hat{\theta}\sin\alpha\sin\beta + \hat{\varphi}\cos\beta$, with $\beta(r)$ satisfying $\beta(0) = 0$ and $\beta(a) = \pi/2$. Note that $\alpha(r) = 0$ corresponds to an achiral ER configuration for a cylinder. However, for finite ξ, we find that there is always a nonzero twist deformation energy, even when requiring $\alpha(r) = 0$ [21, 22].

Since $K_{11} \approx K_{33}$ for 5CB, we also consider $K_{11} = K_{33} = K$ and seek $\alpha(r)$ and $\beta(r)$ that are solutions to the Euler-Lagrange equations for different values of ξ and K_{22}/K. For a cylinder, $K_{22}/K > 0.27$ corresponds to the ER configuration, while $K_{22}/K < 0.27$ results in the chiral TER configuration [11]. We find that the value of K_{22}/K below which the $\alpha = 0$ configuration is unstable depends quadratically on $1/\xi$. This indicates that the region where curvature destabilizes the untwisted ER configuration against the TER configuration broadens with decreasing ξ [21]. These two findings support the idea that not only does geometry induce twist, but that it can also be used to control it.

To further test our hypothesis, and since we cannot measure the twist directly using waveguiding measurements, as the TER structure does not satisfy the required Mauguin criterion [10, 23], we use Jones Calculus [23, 24] to simulate crossed-polarized textures for a toroidal TER configuration. We use an ansatz formed by coupling a doubly-twisted director field in a torus with the ER director field in a cylinder in the one-constant approximation. In the toroidal coordinate system, this ansatz is $\mathbf{n} = \hat{r}\sin(\Omega) + \hat{\theta}\cos(\Omega)\frac{\omega\rho\xi}{\xi-\rho\cos\theta} + \hat{\varphi}\cos(\Omega)\sqrt{1-\left(\frac{\omega\rho\xi}{\xi-\rho\cos\theta}\right)^2}$, where $\rho = r/a$, $\Omega = 2\arctan(\rho)$, and ω governs the amount of twist in the director field. We produce textures for a variety of ξ and twist angles, τ, where $\tau = 2\arcsin\omega$ is the angle between the doubly-twisted portion of the director along the line joining points in the circular cross section at $(r = a, \theta = \pi/2)$ and $(r = a, \theta = 3\pi/2)$ [10]. Example textures in a torus with $\xi = 5$ for twist angle $\tau = 0°$ and $\tau = 47°$ are shown in Figs. 5(a,b), respectively. We measure the intensity profile for each texture [see Fig. 5(c)] and correlate $I_{\max}/I_{\min}$ with τ. We find that $I_{\max}/I_{\min}$ decreases monotonically with increasing τ [see Fig. 5(d)], indicating that $I_{\max}/I_{\min}$ is a proxy for twist and validating our earlier hypothesis that twist decreases with increasing ξ.

Our data then suggests that the twist is induced by the geometry of the torus. To further confirm this, we consider 5CB under homeotropic anchoring in bent glass capillaries, as seen in the bright-field image of an example capillary in Figure 4(b). As with the toroids, we consider a crossed-polarized image and measure the intensity profile across the capillary in regions where the capillary axis is parallel to either P or A. By rotating P and A, we can interrogate different regions in the same capillary; we demonstrate this for the two example highlighted regions in Fig. 4(b). A crossed-polarized image for both regions is shown in Figs. 4(c,d), where P and

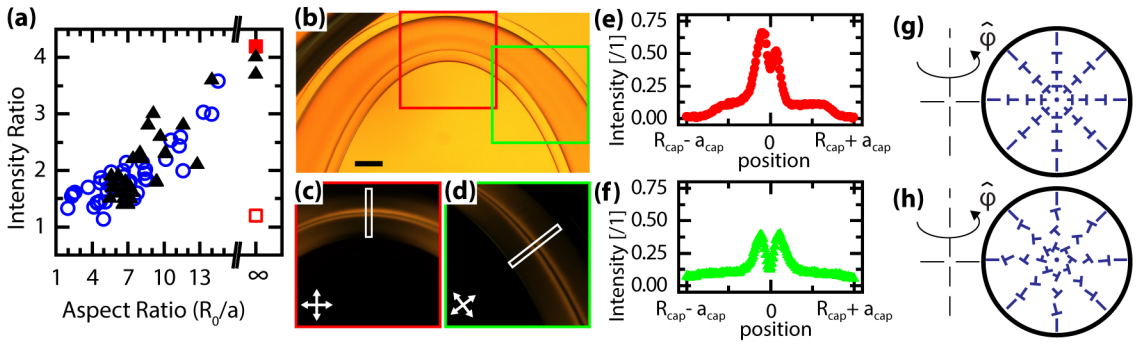

FIG. 4. (a), Intensity ratio, $I_{\max}/I_{\min}$, as a function of the aspect ratio for the homeotropic nematic structures in this work: toroidal droplets filled with 5CB (open circles), a straight cylindrical capillary filled with SSY in the transient ER configuration (filled square) and stable TER configuration (open square), and bent and straight cylindrical capillaries filled with 5CB (triangles). An infinite aspect ratio corresponds to a straight cylindrical capillary. (b), Bright-field microscopy image of a bent cylindrical capillary filled with 5CB under homeotropic anchoring. Scale bar is 200 µm. (c,d), Crossed-polar microscopy images of the highlighted regions in (b), with the polarizer and analyzer orientations indicated schematically in the bottom-left of each image. (e,f) Grayscale intensity profiles across the capillary for the highlighted regions in (c,d), respectively. (g,h), Cross-section director schematic of an ER and a TER configuration, respectively, in a toroidal droplet.

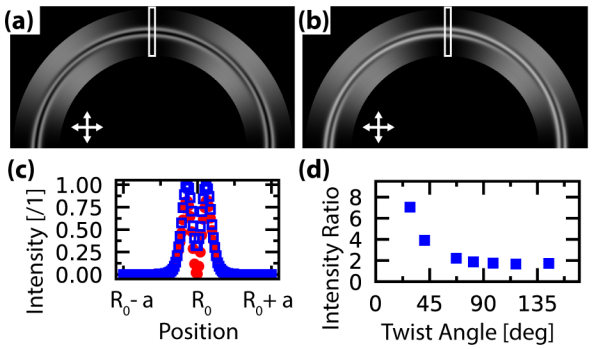

FIG. 5. (a,b), The upper half of simulated crossed-polar images of an ER and TER configuration, respectively, in a torus. The twist angle in (b) is 47°. (c), Intensity profiles for the (circles, open squares) highlighted regions of the tori in (a, b), respectively. (d), Intensity ratio, $I_{\max}/I_{\min}$, as a function of twist angle for the simulated crossed-polar images of TER configurations in a torus.

A have been rotated in each image to align with a portion of the capillary axis. The intensity profiles taken across the highlighted portion of Figs. 4(c,d) are plotted in Figs. 4(e,f) and have $I_{\max}/I_{\min} \approx 1.8$ and $I_{\max}/I_{\min} \approx 3.0$, respectively.

For the example crossed-polarized images in Figs. 4(c,d), we calculate the associated local aspect ratio, $\xi_{\text{local}} = R_{\text{cap}}/a_{\text{cap}}$, with R_{cap} the radius of curvature of the bent capillary axis at the highlighted region of interest and a_{cap} the radius of the capillary [18]. We find $\xi_{\text{local}} = 6.8$ and $\xi_{\text{local}} = 9.1$, respectively. We plot the measurements of $I_{\max}/I_{\min}$ as a function of ξ_{local} for multiple bent capillaries [triangles, Fig. 4(a)], and see that the data from the capillaries fall on top of the data from our toroidal droplets. This clearly indicates that the amount of twist is determined solely by the local geometry. From this perspective, ξ can be seen as a dimensionless parameter locally comparing the relevant curvatures; a gives the radius of curvature in the bend distortion inherent to an ER configuration, while R_0 is the radius of curvature of the additional distortions induced by bending the capillary. Bending the capillary breaks the cylindrical symmetry of both the bend and splay distortions in the ER configuration, introducing a dependence on θ. This can be easily seen by realizing that bending the capillary causes the splay and bend distortions to increase near $\theta = 0$ and decrease near $\theta = \pi$. The aspect ratio in a sense details the magnitude of the asymmetry in these distortions: as ξ decreases, the asymmetry between the distortions near $\theta = 0$ and those near $\theta = \pi$ grows, resulting in the twist distortion becoming more energetically favorable. For the 5CB used in this work, with $K_{11} \approx K_{22} \approx K_{33}$, this asymmetry causes the ER configuration to become unstable with respect to the TER configuration [Figs. 4(g,h)].

In combination with prior results showing that ξ dictates the amount of twist in NLC confined to toroids with planar anchoring, our results in toroids with homeotropic anchoring show that the ability of the confinement geometry to affect the amount of twist is general and does not depend on the specific anchoring. In both scenarios, the key is

$\xi = \kappa_{\text{tube}}/\kappa_{\text{ring}} = R_o/a$, a ratio of curvatures. Since ξ characterizes the local geometry, a gradient in ξ induces a gradient in the amount of twist in a TER configuration. Apart from studies of spontaneous reflection symmetry breaking, chiral nematics are key ingredients in experimental studies of knot theory [25–27], of topological solitons in ordered fields [28, 29], and for controlled self-assembly of colloids dispersed in NLC [30, 31]. Our approach generates a chiral state in NLC without either imposing a predefined pitch through adding a chiral dopant to the NLC [32], or patterning a specified amount of twist through the boundary conditions, as in a twisted nematic cell [23]. Furthermore, we emphasize that the ability to generate a chiral twist gradient, defined as a continuous change in space in the magnitude of the twist, is new and could be exploited in fundamental work addressing twisted states. In addition, our theoretical approach to the problem uses a reasonable ansatz and is just the beginning of other more general approaches that would allow quantitatively determining the role of geometry in the twisted state of homeotropic tori and in other less symmetric objects.

This work was supported by the National Science Foundation (DMR-1609841). PWE and AFN also acknowledge funding from the FLAMEL program (NSF DGE-1258425).

---

* These two authors contributed equally

[1] P. M. Chaikin and T. C. Lubensky, *Principles of condensed matter physics* (Cambridge university press, 2000).

[2] C. M. Soukoulis and M. Wegener, Nature Photonics **5**, 523 (2011).

[3] L. E. Hough, M. Spannuth, M. Nakata, D. A. Coleman, C. D. Jones, G. Dantlgraber, C. Tschierske, J. Watanabe, E. Körblova, and D. M. Walba, Science **325**, 452 (2009).

[4] R. D. Williams, Journal of physics A: mathematical and general **19**, 3211 (1986).

[5] O. Lavrentovich and V. V. Sergan, Il Nuovo Cimento D **12**, 1219 (1990).

[6] J. Pang and N. A. Clark, Physical Review Letters **73**, 2332 (1994).

[7] P. S. Drzaic, Liquid Crystals **26**, 623 (1999).

[8] P. Prinsen and P. van der Schoot, Journal of Physics: Condensed Matter **16**, 8835 (2004).

[9] J. Jeong, Z. S. Davidson, P. J. Collings, T. C. Lubensky, and A. Yodh, Proceedings of the National Academy of Sciences **111**, 1742 (2014).

[10] E. Pairam, J. Vallamkondu, V. Koning, B. C. van Zuiden, P. W. Ellis, M. A. Bates, V. Vitelli, and A. Fernandez-Nieves, Proceedings of the National Academy of Sciences **110**, 9295 (2013).

[11] J. Jeong, L. Kang, Z. S. Davidson, P. J. Collings, T. C. Lubensky, and A. Yodh, Proceedings of the National Academy of Sciences **112**, E1837 (2015).

[12] Z. S. Davidson, L. Kang, J. Jeong, T. Still, P. J. Collings, T. C. Lubensky, and A. Yodh, Physical Review E **91**, 050501 (2015).

[13] K. Nayani, R. Chang, J. Fu, P. W. Ellis, A. Fernandez-Nieves, J. O. Park, and M. Srinivasarao, Nature Communications **6** (2015).

[14] K. Nayani, J. Fu, R. Chang, J. O. Park, and M. Srinivasarao, Proceedings of the National Academy of Sciences , 201614620 (2017).

[15] V. Koning, B. C. van Zuiden, R. D. Kamien, and V. Vitelli, Soft Matter **10**, 4192 (2014).

[16] P. Cladis and M. Kléman, Journal de Physique **33**, 591 (1972).

[17] C. Williams, P. Pierański, and P. E. Cladis, Physical Review Letters **29**, 90 (1972).

[18] See Supplemental Material at [URL] for more information on the experimental methods.

[19] J. M. Brake and N. L. Abbott, Langmuir **18**, 6101 (2002).

[20] We convert the color image to grayscale using a common weighted sum of the red (R), green (G), and blue (B) channels: 0.29889*R + 0.5870*G + 0.1140*B [38].

[21] See Supplemental Material at [URL] for more information on the calculations.

[22] J. P. McInerney, P. W. Ellis, R. D. Zeb, A. Fernandez-Nieves, and E. A. Matsumoto, To be submitted.

[23] P. Yeh and C. Gu, *Optics of liquid crystal displays*, Vol. 67 (John Wiley and Sons, 2010).

[24] R. Ondris-Crawford, E. P. Boyko, B. G. Wagner, J. H. Erdmann, S. Žumer, and J. W. Doane, Journal of Applied Physics **69**, 6380 (1991).

[25] U. Tkalec, M. Ravnik, S. Čopar, S. Žumer, and I. Muševič, Science **333**, 62 (2011).

[26] S. Čopar, U. Tkalec, I. Muševič, and S. Žumer, Proceedings of the National Academy of Sciences **112**, 1675 (2015).

[27] T. Orlova, S. J. Aßhoff, T. Yamaguchi, N. Katsonis, and E. Brasselet, **6**, 7603 (2015).

[28] G. Posnjak, S. Čopar, and I. Muševič, Scientific Reports **6**, 26361 (2016).

[29] P. J. Ackerman and I. I. Smalyukh, Physical Review X **7**, 011006 (2017).

[30] Y. Yuan, A. Martinez, B. Senyuk, M. Tasinkevych, and I. I. Smalyukh, Nature Materials **17**, 71 (2018).

[31] I. I. Smalyukh, Annual Review of Condensed Matter Physics (2017).

[32] P. G. de Gennes and J. Prost, *The physics of liquid crystals* (Oxford University Press, New York, 1995).

[33] E. Pairam, H. Le, and A. Fernandez-Nieves, Physical Review E **90**, 021002 (2014).

[34] K. Hiltrop and H. Stegemeyer, Molecular Crystals and Liquid Crystals **49**, 61 (1978).

[35] V. R. Horowitz, L. A. Janowitz, A. L. Modic, P. A. Heiney, and P. J. Collings, Physical Review E **72**, 041710 (2005).

[36] R. D. Kamien, Reviews of Modern Physics **74**, 953 (2002).
[37] P. W. Ellis, D. J. G. Pearce, Y.-W. Chang, G. Goldsztein, L. Giomi, and A. Fernandez-Nieves, Nature Physics (2017).
[38] *Studio encoding paramters of digital television for standard 4:3 and wide-screen 16:9 aspect ratios*, Recommendation ITU-R BT.601-7 (2011).